Available online at www.sciencedirect.com
SCIENCE DIRECT
Journal of Solid State Chemistry 179 (2006) 2376–2385
JOURNAL OF SOLID STATE CHEMISTRY
www.elsevier.com/locate/jssc

Structural, magnetic, and spectroscopic studies of YAgSn, TmAgSn, and LuAgSn

C. Peter Sebastian[a], Hellmut Eckert[b], Constanze Fehse[b], Jon P. Wright[c], J. Paul Attfield[d], Dirk Johrendt[e], Sudhindra Rayaprol[a], Rolf-Dieter Hoffmann[a], Rainer Pöttgen[a,*]

[a]*Institut für Anorganische und Analytische Chemie and NRW Graduate School of Chemistry, Universität Münster, Corrensstrasse 30, D-48149 Münster, Germany*
[b]*Institut für Physikalische Chemie and NRW Graduate School of Chemistry, Universität Münster, Corrensstrasse 30, D-48149 Münster, Germany*
[c]*European Synchrotron Radiation Facility, BP 220, F-38043 Grenoble Cedex, France*
[d]*Centre for Science at Extreme Conditions, University of Edinburgh, Erskine Williamson Building, King's Buildings, Mayfield Road, Edinburgh, EH9 3JZ, UK*
[e]*Department Chemie und Biochemie, Ludwig-Maximilians-Universität München, Butenandtstrasse 5–13 (Haus D), 81377 München, Germany*

Received 22 March 2006; received in revised form 12 April 2006; accepted 16 April 2006
Available online 12 May 2006

Abstract

The rare earth–silver–stannides YAgSn, TmAgSn, and LuAgSn were synthesized from the elements by arc-melting and subsequent annealing. The three stannides were investigated by X-ray powder and single-crystal diffraction: NdPtSb type, $P6_3mc$, $Z = 2$, $a = 468.3(1)$, $c = 737.2(2)$ pm, w$R_2 = 0.0343$, 353 F^2 values, 12 variables for YAgSn, and ZrNiAl type, $P\bar{6}2m$, $a = 726.4(2)$, $c = 443.7(1)$ pm, w$R_2 = 0.0399$, 659 F^2 values, 15 variables for TmAgSn, and $a = 723.8(2)$, $c = 442.47(9)$ pm, w$R_2 = 0.0674$, 364 F^2 values, 15 variables for LuAgSn. Besides conventional laboratory X-ray data with monochromatized Mo radiation, the structures were also refined on the basis of synchrotron data with $\lambda = 48.725$ pm, in order to clarify the silver–tin ordering more precisely. YAgSn has puckered, two-dimensional [AgSn] networks with Ag–Sn distances of 278 pm, while the [AgSn] networks of TmAgSn and LuAgSn are three-dimensional with Ag–Sn distances of 279 and 284 pm for LuAgSn. Susceptibility measurements indicate Pauli paramagnetism for YAgSn and LuAgSn. TmAgSn is a Curie–Weiss paramagnet with an experimental magnetic moment of 7.2 μ_B/Tm. No magnetic ordering is evident down to 2 K. The local environments of the tin sites in these compounds were characterized by ^{119}Sn Mössbauer spectroscopy and solid-state NMR (in YAgSn and LuAgSn), confirming the tin site multiplicities proposed from the structure solutions and the absence of Sn/Ag site disordering. Mössbauer quadrupolar splittings were found in good agreement with calculated electric field gradients predicted quantum chemically by the WIEN2k code. Furthermore, an excellent correlation was found between experimental ^{119}Sn nuclear magnetic shielding anisotropies (determined via MAS-NMR) and calculated electric field gradients. Electronic structure calculations predict metallic properties with strong Ag–Sn bonds and also significant Ag–Ag bonding in LuAgSn.

Keywords: Stannides; Solid-state NMR; Mössbauer spectroscopy

1. Introduction

The equiatomic rare earth (*RE*)–silver–stannides *RE*AgSn have been intensively studied in recent years with respect to their crystal chemistry and physical properties [1–34]. Depending on the valence state and size of the rare earth element, the *RE*AgSn stannides crystallize with different structure types. With *RE* = Y, La–Nd, Sm, Gd–Er they crystallize with the hexagonal NdPtSb-type structure, space group $P6_3mc$, a slightly puckered, version of AlB_2 [35] with ordered Ag_3Sn_3 hexagons. The rare earth atoms are all in a stable trivalent state in the latter stannides.

EuAgSn [7,12,26] and YbAgSn [1,10,13,20,21,28] contain divalent europium and ytterbium, and their crystal structures differ from those of the early rare earth elements.

*Corresponding author. Tel.: +49 251 83 36001; fax: +49 251 83 36002.
E-mail addresses: eckerth@uni-muenster.de (H. Eckert), pottgen@uni-muenster.de (R. Pöttgen).

0022-4596/$ - see front matter © 2006 Elsevier Inc. All rights reserved.
doi:10.1016/j.jssc.2006.04.038

The europium compound crystallizes with the orthorhombic KHg_2-type structure, space group *Imma*, and YbAgSn adopts the YbAgPb type, space group $P\bar{6}m2$, with a planar and two puckered Ag_3Sn_3 hexagons. Nevertheless, the three different structure types are all superstructures of the aristotype AlB_2 [35].

Most of the *RE*AgSn stannides show antiferromagnetic ordering at low temperatures and the magnetic structures have been determined from neutron powder data [4,17]. For the refinement of the nuclear structures, the fits of the neutron data were slightly better for the ordered NdPtSb-type arrangement. Magnetization data indicated interesting metamagnetic behavior for the neodymium, terbium [5], and holmium [6] compounds. A very interesting observation is noticed in the ^{119}Sn Mössbauer spectra [7,20,23,26,29,31,33,34]. The isomer shift decreases from the lanthanum ($\delta = 1.85$ mm/s) to the erbium ($\delta = 1.67$ mm/s) compound, indicating a decrease of the *s* electron density at the tin nuclei. This is directly related to the trend of the electronegativities of the rare earth elements. At low temperatures, in the magnetically ordered regimes, the ^{119}Sn spectra show significant transferred magnetic hyperfine fields.

With the smaller rare earth elements thulium, lutetium, and scandium, so far no *RE*AgSn stannides have been reported. We were interested in these compounds in the course of our systematic ^{119}Sn solid-state NMR investigations of ternary stannides with the diamagnetic rare earth elements [36]. Herein we report on the successful synthesis of YAgSn, TmAgSn, and LuAgSn in X-ray pure form. The new stannides TmAgSn and LuAgSn crystallize with the ZrNiAl type, space group $P\bar{6}2m$. With the smallest rare earth element scandium, the TiFeSi type is formed [37]. The latter is a superstructure of the ZrNiAl type upon doubling of one subcell axis [38].

A common problem of all ternary silver stannides is the correct site assignment for the silver and tin atoms. Since silver and tin differ by only three electrons, it is difficult to distinguish the silver and tin sites even in high-quality single-crystal X-ray data sets. We have therefore investigated the stannides YAgSn, TmAgSn, and LuAgSn also by single-crystal synchrotron data, using a radiation of 48.725 pm, near the silver edge. Together with ^{119}Sn solid-state NMR data, a definite assignment of these sites was possible.

2. Experimental

2.1. Synthesis

The starting materials for the preparation of YAgSn, TmAgSn, and LuAgSn were ingots of the rare earth elements (Johnson-Matthey and Kelpin), silver wire (Degussa-Hüls, Ø 1 mm), and tin granules (Merck), all with stated purities better than 99.9%. In a first step, small pieces of the rare earth ingots were arc-melted [39] to small buttons under an argon atmosphere of ca. 600 mbar. The argon was purified before over titanium sponge (870 K), silica gel, and molecular sieves. The small rare earth buttons were then mixed with pieces of the silver wire and the tin granules in the ideal 1:1:1 atomic ratios and arc-melted three times in order to get homogenous samples. The total weight losses after the arc-melting procedures were always smaller than 0.5 wt%. In a second step the samples were sealed in evacuated silica tubes and annealed at 970 K for 10 days. YAgSn, TmAgSn, and LuAgSn were obtained as light gray buttons in amounts of ca. 1 g. The samples are stable in moist air over a period of months. Single crystals of these stannides exhibit metallic lustre.

2.2. X-ray powder data

The samples were characterized through Guinier powder patterns with α-quartz ($a = 491.30$, $c = 540.46$ pm) as an internal standard and Cu $K\alpha_1$ radiation. The Guinier camera was equipped with an imaging plate system (Fujifilm, BAS-1800). The experimental patterns were compared to calculated ones [40], taking the atomic sites derived from the single-crystal data. All samples were phase pure on the level of X-ray powder diffraction. After correct indexing, the hexagonal lattice parameters (Table 1) were refined by least-squares calculations. The lattice parameters determined on the single-crystal diffractometers were in good agreement with the powder data, however, only the powder data that have been refined with internal standard are listed.

2.3. Laboratory single-crystal X-ray data

Irregularly shaped crystals of YAgSn, TmAgSn, and LuAgSn were directly selected from the crushed samples. They were glued to small quartz fibers using bees wax and then checked by Laue photographs on a Buerger camera, equipped with the same Fujifilm, BAS-1800 imaging plate technique. The good quality crystals were then used for the intensity data collections on a Nonius CAD4 four circle diffractometer, equipped with graphite monochromatized Mo $K\alpha$ radiation and a scintillation counter with pulse-height discrimination. Scans were taken in the $\omega/2\theta$ mode and empirical absorption corrections were applied on the basis of psi-scan data, followed by spherical absorption corrections. All relevant crystallographic data for these data collections and evaluations are listed in Table 1.

2.4. Single-crystal synchrotron data

Silver and tin are difficult to distinguish by normal (non-resonant) X-ray diffraction, or by neutron diffraction (scattering lengths are $b_{Ag} = 6.02$ and $b_{Sn} = 6.22$ fm). Resonant X-ray diffraction can provide a good contrast between similar elements by exploiting the large changes in anomalous dispersion coefficients close to elemental absorption edges. The Ag K and Sn K edges have energies of 25 514 and 29 200 eV, respectively, so an energy just

Table 1
Crystal data and structure refinement for YAgSn, TmAgSn, and LuAgSn (CAD4 X-ray data, Mo radiation, $\lambda = 71.073$ pm)

Empirical formula	YAgSn	TmAgSn	LuAgSn
Molar mass (g/mol)	315.47	395.49	401.53
Unit cell dimensions	$a = 468.3(1)$ pm	726.4(2) pm	723.8(2) pm
(Guinier powder data)	$c = 737.2(2)$ pm	443.7(1) pm	442.47(9) pm
	$V = 0.1400$ nm^3	0.2028 nm^3	0.2008 nm^3
Space group	$P6_3mc$	$P\bar{6}2m$	$P\bar{6}2m$
Structure type	NdPtSb	ZrNiAl	ZrNiAl
Pearson symbol	hP6	hP9	hP9
Calculated density (g/cm^3)	7.48	9.72	9.96
Crystal size (μm^3)	$45 \times 65 \times 90$	$20 \times 35 \times 80$	$10 \times 20 \times 50$
Transm. ratio (max/min)	2.65	2.21	3.89
Absorption coefficient (mm^{-1})	36.0	48.5	52.7
$F(0\,0\,0)$	272	498	504
θ range	5°–40°	3°–45°	3°–35°
Range in $h\,k\,l$	± 8, ± 8, $-13/+11$	± 14, ± 14, $0/+8$	± 11, ± 11, $0/+7$
Total no. reflections	3061	3596	1945
Independent reflections	353 ($R_{int} = 0.0767$)	659 ($R_{int} = 0.0798$)	364 ($R_{int} = 0.1119$)
Reflections with $I > 2\sigma(I)$	307 ($R_\sigma = 0.0300$)	626 ($R_\sigma = 0.0384$)	353 ($R_\sigma = 0.0526$)
Data/parameters	353/12	659/15	364/15
Goodness-of-fit on F^2	1.031	1.013	1.128
Weighting scheme[a]	$a = 0.0125$	$a = 0.0100$	$a = 0.0267$
	$b = 0$	$b = 0$	$b = 0$
Final R indices [$I > 2\sigma(I)$]	$R_1 = 0.0196$	$R_1 = 0.0231$	$R_1 = 0.0279$
	$wR_2 = 0.0327$	$wR_2 = 0.0386$	$wR_2 = 0.0666$
R indices (all data)	$R_1 = 0.0308$	$R_1 = 0.0267$	$R_1 = 0.0295$
	$wR_2 = 0.0343$	$wR_2 = 0.0399$	$wR_2 = 0.0674$
BASF	0.37(2)	0.42(1)	0.26(2)
Extinction coefficient	0.020(1)	0.0087(3)	0.0092 (9)
Largest diff. peak and hole (Ae/Å^3)	0.86/–1.03	3.05/–1.68	5.02/–1.40

[a]Weight $= 1/[\sigma^2 (F_o^2) + (a \cdot P)^2 + b \cdot P]$, where $P = 1/3 \max(0, F_o^2) + 2/3\, F_c^2$.

below the Ag K edge will give a large negative value of f' (the real part of the anomalous scattering) while the sample absorption remains low. This strategy has been used previously to quantify the distribution of Fe and Ni in $Fe_2NiO_2BO_3$ [41].

Synchrotron X-ray diffraction data from the above crystals of YAgSn, TmAgSn, and LuAgSn were collected on beamline ID11 at ESRF. Diffraction images were collected using an ESRF Frelon CCD camera via the rotation method with a single vertical rotation axis. The experiment was repeated with wavelengths of 15.5 pm (80 keV) and 48.725 pm (25449 eV; 65 eV below the silver edge) at room temperature. Images were converted to Bruker AXS format for indexing using the "Smart" program [42] and integration using the "Saint" program [42]. Empirical absorption corrections were performed using "Sadabs" [43]. The real (f') and imaginary (f'') anomalous dispersion coefficients used for the refinements were $f'_{Ag} = -7.070$ e/atom, $f''_{Ag} = 0.554$ e/atom, $f'_{Sn} = -1.682$ e/atom, and $f''_{Sn} = 0.722$ e/atom. Experimental and refinement details are shown in Tables 2 and 3.

2.5. Scanning electron microscopy

The single crystals investigated on the diffractometers and the bulk samples were analyzed using a LEICA 420 I scanning electron microscope with Y, TmF_3, LuF_3, Ag, and Sn as standards. No impurity elements heavier than sodium were observed. The compositions determined by EDX (36±3 at% Y: 31±3 at% Ag: 33±3 at% Sn, 32±2 at% Tm: 33±2 at% Ag: 35±2 at% Sn, and 33±1 at% Lu: 33±1 at% Ag: 34±1 at% Sn) are in good agreement with the ideal 1:1:1 composition. The standard uncertainties account for the various point analyses.

2.6. Magnetic properties and ^{119}Sn Mössbauer spectroscopy

The magnetic measurements of *RE*AgSn (*RE* = Y, Tm, and Lu) were carried out using the AC magnetic susceptibility option of a Quantum Design Physical Property Measurement System. The samples were enclosed in gelatin capsules and attached to the sample rod assembly. Samples were cooled to the lowest attainable temperature (2 K) in zero field. The susceptibility, $\chi(T)$, was measured while warming the samples in the applied field.

A $Ca^{119m}SnO_3$ source was available for the ^{119}Sn Mössbauer spectroscopic investigations. The samples were placed within thin-walled PVC containers at a thickness that corresponds to a tin quantity of about 10 mg Sn/cm^2. A palladium foil of 0.05 mm thickness was used to reduce the tin K X-rays concurrently emitted by this source. The

Table 2
Crystal data and structure refinement for YAgSn, TmAgSn and LuAgSn (ESRF synchrotron data, $\lambda = 48.725$ pm).

Empirical formula	YAgSn	TmAgSn	LuAgSn
Molar mass (g/mol)	315.47	395.49	401.53
Unit cell dimensions	$a = 468.3(1)$ pm	726.4(2) pm	723.8(2) pm
(Guinier powder data)	$c = 737.2(2)$ pm	443.7(1) pm	442.47(9) pm
	$V = 0.1400$ nm^3	0.2028 nm^3	0.2008 nm^3
Space group	$P6_3mc$	$P\bar{6}2m$	$P\bar{6}2m$
Structure type	NdPtSb	ZrNiAl	ZrNiAl
Pearson symbol	hP6	hP9	hP9
Calculated density (g/cm^3)	7.48	9.72	9.96
Crystal size (μm^3)	$45 \times 65 \times 90$	$20 \times 35 \times 80$	$10 \times 20 \times 50$
Absorption coefficient (mm^{-1})	19.3	25.8	28.2
$F(0\,0\,0)$	272	498	504
θ range	3°–20°	2°–33°	2°–33°
Range in $h\,k\,l$	±5, ±6, −5/9	−7/+12, −15/+13, −8/+9	−15/+11, −15/+10, −9/+7
Total no. reflections	551	3494	3732
Independent reflections	125 ($R_{int} = 0.0340$)	736 ($R_{int} = 0.0358$)	811 ($R_{int} = 0.0346$)
Reflections with $I > 2\sigma(I)$	113 ($R_\sigma = 0.0299$)	728 ($R_\sigma = 0.0267$)	798 ($R_\sigma = 0.0281$)
Data/parameters	125/12	736/15	811/15
Goodness-of-fit on F^2	1.283	1.090	1.092
Weighting scheme[a]	$a = 0.0222$	$a = 0.0621$	$a = 0.0244$
	$b = 0.1066$	$b = 0.5835$	$b = 0.8418$
Final R indices [$I > 2\sigma(I)$]	$R_1 = 0.0204$	$R_1 = 0.0312$	$R_1 = 0.0200$
	$wR_2 = 0.0468$	$wR_2 = 0.0812$	$wR_2 = 0.0500$
R indices (all data)	$R_1 = 0.0228$	$R_1 = 0.0314$	$R_1 = 0.0206$
	$wR_2 = 0.0478$	$wR_2 = 0.0813$	$wR_2 = 0.0503$
BASF	0.5(1)	0.42(3)	0.30(2)
Extinction coefficient	0.05(1)	0.063(8)	0.020(3)
Largest diff. peak and hole (e/Å^3)	1.18/–1.24	6.97/–3.13	3.13 /–2.52

[a]Weight $= 1/[\sigma^2 (F_o^2) + (a \cdot P)^2 + b \cdot P]$ where $P = 1/3$ max $(0, F_o^2) + 2/3\ F_c^2$.

measurements were conducted in the usual transmission geometry at $T = 78$ K. The spectra were fitted to Lorentzian doublets, arising from nuclear electric quadrupolar splitting. Appropriate starting values for these fits were quantum-chemical calculations of the electric field gradients using the WIEN2k program code [44].

2.7. ^{119}Sn solid-state NMR

^{119}Sn NMR spectra were recorded at 149.1 MHz, on a Bruker DSX 400 spectrometer equipped with a 4 mm MAS-NMR probe (magic-angle spinning). Spectra were taken on samples spinning at a rate of 12 kHz, using 90° pulses of length of 2.2 and 2.6 μs for YAgSn and LuAgSn, respectively, followed by a relaxation delay of 0.5 s. Chemical shifts are reported relative to tetramethyltin, using tin(IV)oxide as a secondary reference. To minimize undesirable effects of probe detuning and sample heating of these highly metallic samples, the finely ground powders were mixed with silica in a 1:1 mass ratio. Using the DMFIT routine [45], the MAS sideband patterns were fitted to yield the anisotropic shielding tensor components, using the following definitions:

$$\delta_{CS} = -\left(\sigma_{ZZ}^{PAS} - \sigma_{iso}\right), \quad \eta_{CS} = \frac{\sigma_{YY}^{PAS} - \sigma_{XX}^{PAS}}{\sigma_{ZZ}^{PAS} - \sigma_{iso}},$$

$$\sigma_{iso} = \frac{1}{3}\left(\sigma_{XX}^{PAS} + \sigma_{YY}^{PAS} + \sigma_{ZZ}^{PAS}\right),$$

where the superscript "PAS" refers to the principal axis system of the shielding tensor.

2.8. Electronic structure calculations

Self-consistent DFT band structure calculations were performed using the LMTO-method in its scalar-relativistic version (program TB-LMTO-ASA) [46]. Detailed descriptions are given elsewhere [47,48]. Reciprocal space integrations were performed with the tetrahedron method [49] using 245 irreducible k-points out of 2197 (grid of $13 \times 13 \times 13$) in the hexagonal Brillouin zone. The basis set consisted of Lu-6s/{6p}/5d/4f, Ag-5s/5p/4d/{4f} and Sn-5s/5p/{5d/4f}. Orbitals given in parenthesis were downfolded [50]. In order to achieve space filling within the atomic sphere approximation, interstitial spheres are introduced to avoid too large overlap of the atom-centered spheres. The empty spheres positions and radii were calculated automatically. We did not allow overlaps of more than 15% for any two atom-centered spheres. The COHP method (Crystal Orbital Hamilton Population) was used for the bond analysis [51]. COHP gives the energy contributions of all electronic states for a selected bond. The values are negative for bonding and positive for antibonding interactions. With respect to the COOP diagrams, we plot –COHP(E) to get positive values for bonding states.

Table 3
Atomic coordinates and isotropic displacement parameters (pm^2) of YAgSn, TmAgSn, and LuAgSn.

Atom	*Wyck*	*x*	*y*	*z*	U_{eq}
YAgSn (laboratory X-ray data)					
Y	2*a*	0	0	0.9999(2)	67(1)
Ag	2*b*	2/3	1/3	0.30833(8)	99(2)
Sn	2*b*	2/3	1/3	0.71978(5)	62(2)
YAgSn (synchrotron data)					
Y	2*a*	0	0	0.0013(9)	34(3)
Ag	2*b*	2/3	1/3	0.3081(3)	71(8)
Sn	2*b*	2/3	1/3	0.7196(3)	40(4)
TmAgSn (laboratory X-ray data)					
Tm	3*f*	0.43129(5)	0	0	99(1)
Ag	3*g*	0.75532(8)	0	1/2	132(1)
Sn1	2*d*	2/3	1/3	1/2	85(1)
Sn2	1*a*	0	0	0	119(2)
TmAgSn (synchrotron data)					
Tm	3*f*	0.43131(5)	0	0	63(1)
Ag	3*g*	0.7552(1)	0	1/2	101(1)
Sn1	2*d*	2/3	1/3	1/2	52(1)
Sn2	1*a*	0	0	0	86(2)
LuAgSn (laboratory X-ray data)					
Lu	3*f*	0.4319(1)	0	0	115(2)
Ag	3*g*	0.7550(2)	0	1/2	150(3)
Sn1	2*d*	2/3	1/3	1/2	97(3)
Sn2	1*a*	0	0	0	139(4)
LuAgSn (synchrotron data)					
Lu	3*f*	0.43199(3)	0	0	60(1)
Ag	3*g*	0.75510(9)	0	1/2	93(1)
Sn1	2*d*	2/3	1/3	1/2	45(1)
Sn2	1*a*	0	0	0	85(1)

U_{eq} is defined as one-third of the trace of the orthogonalized U_{ij} tensor.

Table 4
Interatomic distances (pm), calculated with the lattice parameters taken from X-ray powder data of YAgSn, TmAgSn and LuAgSn.

Y:			Tm:			Lu:		
3	Ag	305.0	4	Sn1	309.3	4	Sn1	308.3
3	Sn	315.2	1	Sn2	313.3	1	Sn2	312.6
3	Sn	340.2	2	Ag	323.4	2	Ag	321.9
3	Ag	353.3	4	Ag	351.1	4	Ag	350.3
2	Y	368.6	4	Tm	373.4	4	Lu	371.8
			Ag:			Ag:		
6	Y	468.3	2	Sn1	279.9	2	Sn1	278.8
Ag:								
3	Sn	278.1	2	Sn2	284.3	2	Sn2	283.5
1	Sn	303.3	2	Ag	307.9	2	Ag	307.1
3	Y	305.0	2	Tm	323.4	2	Lu	321.9
3	Y	353.3	4	Tm	351.1	4	Lu	350.3
Sn:			Snl:			Snl:		
3	Ag	278.1	3	Ag	279.9	3	Ag	278.8
1	Ag	303.3	6	Tm	309.3	6	Lu	308.3
			Sn2:			Sn2:		
3	Y	315.2	6	Ag	284.3	6	Ag	283.5
3	Y	340.2	3	Tm	313.3	3	Lu	312.6

All distances within the first coordination spheres are listed. Standard deviations are equal or less than 0.2 pm.

3. Results and discussion

3.1. Structure refinements

First, the structures were determined and refined on the basis of the laboratory X-ray data. For the YAgSn crystal, the systematic extinctions were compatible with space group $P6_3mc$, in agreement with all neutron powder data given by Szytuła for other rare earth elements [4,17]. The starting atomic positions were deduced from an automatic interpretation of direct methods and the structure was refined with anisotropic displacement parameters for all atoms with SHELXL-97 (full-matrix least-squares on F_o^2) [52]. Refinement of the Flack parameter [53,54] indicated twinning by inversion, as usually observed for the non-centrosymmetric LiGaGe/NdPtSb-type intermetallics [35]. We have then introduced the inversion twin matrix and a batch scale factor was refined (Table 1). The refinement then converged to the residuals listed in Table 1 and the atomic parameters and interatomic distances listed in Tables 3 and 4. The silver atoms of YAgSn show the larger dislocation from the subcell mirror plane, similarly to other NdPtSb-type structure compounds [55]. Assignment of the silver and the tin position was performed through a refinement of the occupancy parameters.

The data sets of TmAgSn and LuAgSn showed no systematic extinctions as expected. The atomic parameters of DyAgGe [56] were used as starting values and the two structures were refined with anisotropic displacement parameters for all sites. In a first step, the three sites 3*g*, 2*d*, and 1*a* were refined all with silver atoms. A subsequent refinement of the occupancy parameters for both data sets clearly showed that the 1*a* and 2*d* sites exhibit higher electron density, and consequently these two sites were assigned with tin atoms. We have then obtained full occupancy for these sites. To give an example, for TmAgSn the occupancy parameters were 100.5(4)% for Ag, 99.8(4)% for Sn1, and 100.5(6)% for Sn2. For comparison, a silver site occupied with tin should show an occupancy parameter around 106%. The crystals of TmAgSn and LuAgSn showed also twinning by inversion. The refined positional parameters and interatomic distances are listed in Tables 3 and 4.

Since it is always a difficult task to distinguish silver and tin (three electrons difference) from single-crystal laboratory X-ray studies, further data sets on the same crystals were collected with synchrotron radiation (see Chapter 2.4). The atomic parameters determined from the laboratory X-ray data were used as starting values and the same structure refinements were carried out. The synchrotron data fully confirmed the silver-tin assignments. The refined data are listed in Tables 2–4. Also the refined occupancy parameters (101.3(7)% for Ag, 99.8(6)% for Sn1 and

99.0(7)% for Sn2) for TmAgSn and (100.9(4)% for Ag, 100.0(4)% for Sn1 and 99.7(5)% for Sn2) for LuAgSn reveal full occupancy within two standard uncertainties. The diffraction results are fully supported by ^{119}Sn solid-state NMR spectroscopy, discussed below. Further data on the structure refinements are available.[1]

3.2. Crystal chemistry and chemical bonding

New stannides TmAgSn and LuAgSn have been synthesized and characterized in the series of *RE*AgSn intermetallics. The structure of YAgSn, previously reported by Mazzone et al. [1] on the basis of X-ray powder data was confirmed and more precisely refined from single-crystal data.

YAgSn adopts the NdPtSb structure, with two-dimensional [AgSn] networks as emphasized in Fig. 1. Within the puckered [Ag_3Sn_3] hexagons, the Ag–Sn distances are 278 pm, close to the sum of the covalent radii for silver and tin of 274 pm [57]. The shortest Ag–Sn distance between the layers is at 303 pm, and, if at all, these interactions are only very weak. The dimensionality of such networks is a function of the size of the rare earth element. With the larger rare earth elements these networks are almost flat. The YAgSn structure is another example for an AlB_2-related superstructure. The crystal chemistry of these materials has extensively been discussed in a recent review [35].

With the smaller rare earth elements thulium and lutetium, the *RE*AgSn stannides switch in structure type. TmAgSn and LuAgSn adopt the hexagonal ZrNiAl type as shown in Fig. 2. Both stannides contain two crystallographically independent tin sites in trigonal prismatic coordination. The Sn1 atoms have trigonal prisms formed by the rare earth metal atoms and those of Sn2 are built up from silver atoms. Both types of trigonal prisms are capped on the rectangular faces: [Sn1Lu_6] by three silver atoms and [Sn2Ag_6] by three lutetium atoms, leading to coordination number nine for both tin sites.

The Ag–Sn distances (279–284 pm) are slightly larger for LuAgSn than for YAgSn discussed above, but they are also close to the sum of the covalent radii. We can therefore assume significant Ag–Sn bonding within the three-dimensional [AgSn] networks. The triangular faces of the [Sn2Ag_6] prisms have edge lengths of 307 pm (Ag–Ag), slightly longer than the Ag–Ag distances of 289 in fcc silver [58], and there are certainly also weak Ag–Ag interactions within the [AgSn] networks. For further crystal chemical details on ZrNiAl-related intermetallics we refer to previous literature [59,60].

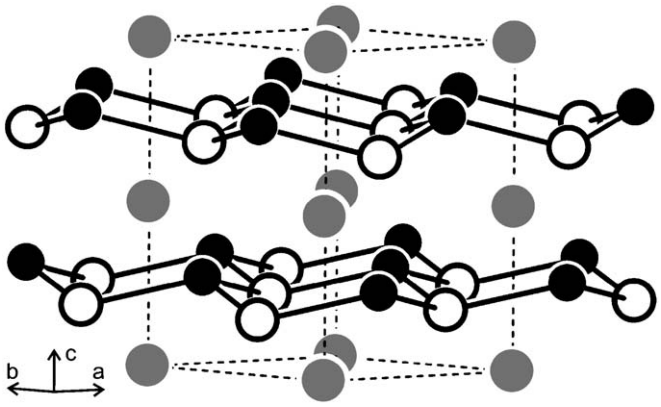

Fig. 1. Crystal structure of YAgSn. Yttrium, silver, and tin atoms are drawn as medium grey, black filled, and open circles, respectively. The two-dimensional [AgSn] networks are emphasized.

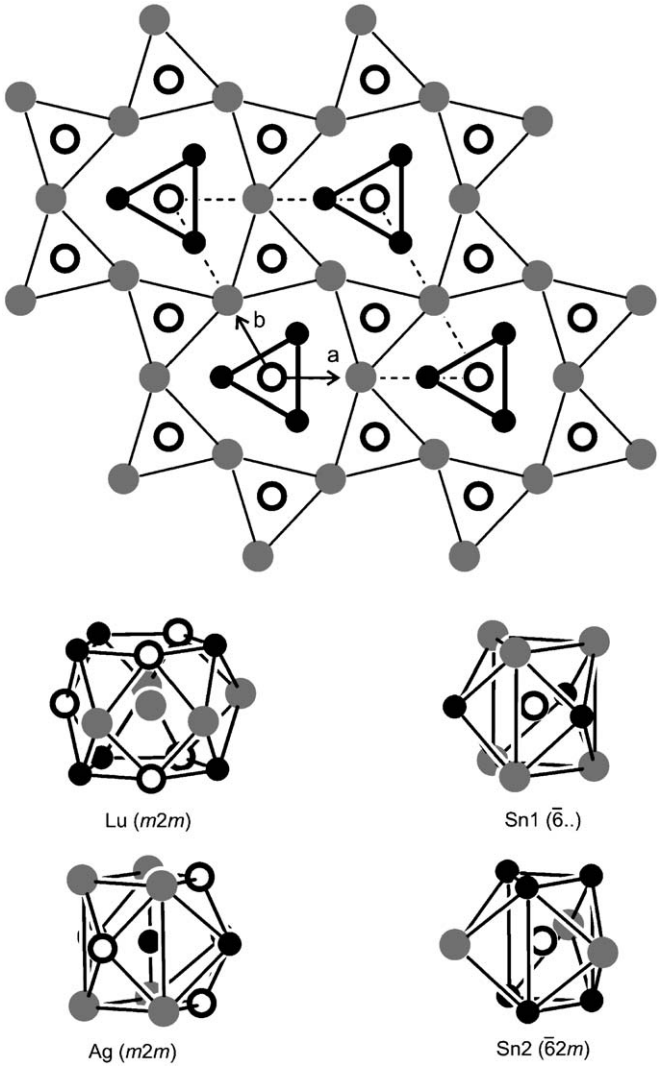

Fig. 2. Projection of the LuAgSn structure onto the *xy* plane (upper drawing). All atoms lie on mirror planes at $z = 0$ (thin lines) and $z = 1/2$ (thick lines). Lutetium, silver, and tin atoms are drawn as medium gray, black, and open circles, respectively. The trigonal prisms around the tin atoms are emphasized. The coordination polyhedra are drawn in the lower part. The site symmetries are indicated.

[1]Details may be obtained from: Fachinformationszentrum Karlsruhe, D-76344 Eggenstein-Leopoldshafen (Germany), by quoting the Registry Nos. CSD–416375 (YAgSn), CSD–416376 (TmAgSn), and CSD–416377 (LuAgSn)

3.3. Electronic structure calculations

We have investigated the electronic structure and chemical bonding in LuAgSn by density of states (DOS) and crystal orbital Hamilton populations (COHP), obtained from self-consistent DFT band structure calculations. We have also checked the conceivable exchange of tin and silver with regard to the total electronic energy at constant volume. The structure as given here (Table 3) is about 2.2 eV/cell lower in energy and represents the correct distribution of silver and tin also from the viewpoint of electronic energy. Fig. 3 shows the total DOS of LuAgSn together with the Ag contribution. The metallic property is clearly discerned even though the DOS at the Fermi level of about 1.25 states eV^{-1} $cell^{-1}$ is rather low. Just below the Fermi energy, we find mainly the 5*p* orbitals of tin, hybridized with the Ag 5*s*. The maxima between −5 and −6 eV correspond to the filled Ag 4*d* shell and also to the strongly localized Lu 4*f* orbitals, which form the sharp peak at −5.5 eV. Below −8 eV the DOS is dominated by the 5*s* orbitals of tin, which also mix with some Ag levels. The COHP diagrams in Fig. 4 illustrate the Ag–Sn and Ag–Ag bonding in LuAgSn. Both curves are scaled to represent one bond each for comparison. As expected, the Ag–Sn bonds are much stronger than the Ag–Ag bonds. The Fermi level just divides the Ag–Sn bonding from the antibonding states and thus an optimal situation is established, as often observed for the primary bonding interactions in solids.

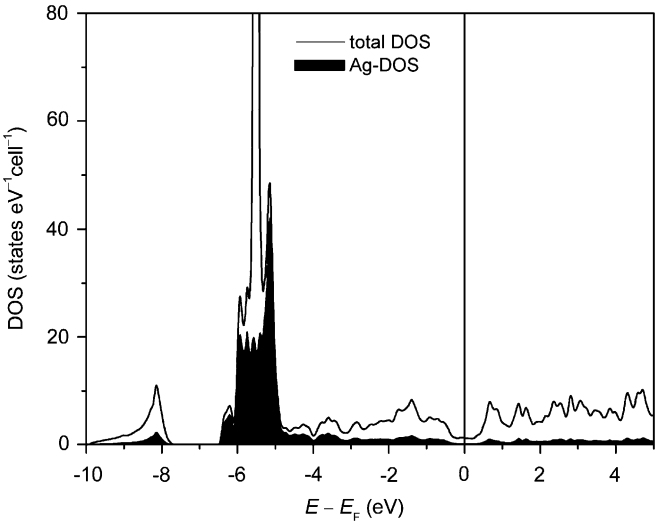

Fig. 3. Total density of states (DOS) of LuAgSn (solid line) and the contribution of the Ag orbitals (black shaded area). The energy zero is taken at the Fermi level.

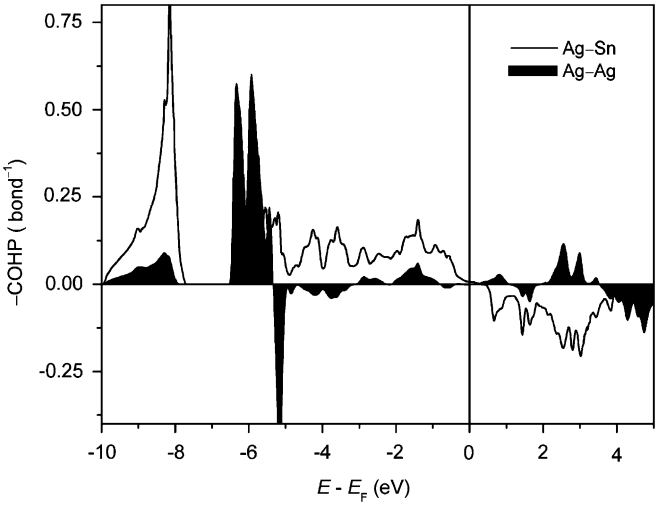

Fig. 4. Crystal orbital Hamiltonian population (COHP) diagrams of LuAgSn. The Ag-Sn COHP is shown as solid line and the Ag-Ag COHP as shaded area. Integrated ICOHP(E_F) values are 1.22 eV/bond (Ag–Sn) and 0.41 eV/bond (Ag-Ag).

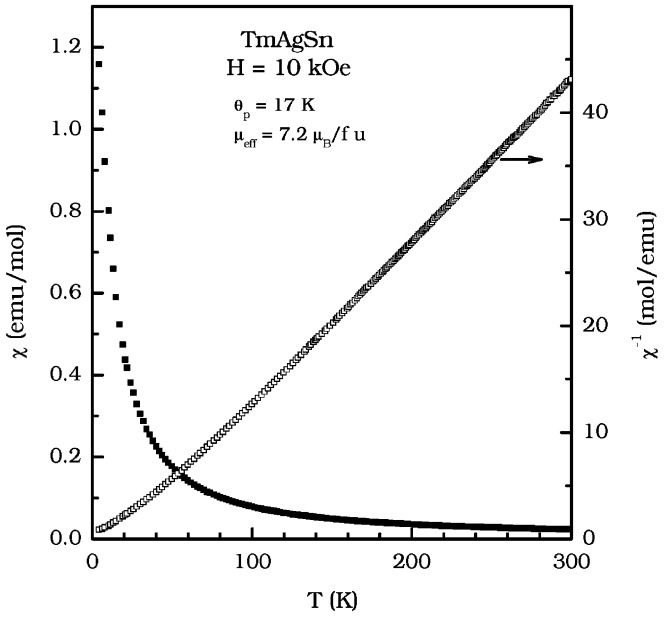

Fig. 5. dc susceptibility (χ) and inverse susceptibility (χ^{-1}) of TmAgSn measured in a field of 10 kOe. The values of the paramagnetic Curie temperature (θ_p) and the effective Bohr magneton number (μ_{eff}) were calculated from the high temperature linear region of χ^{-1}.

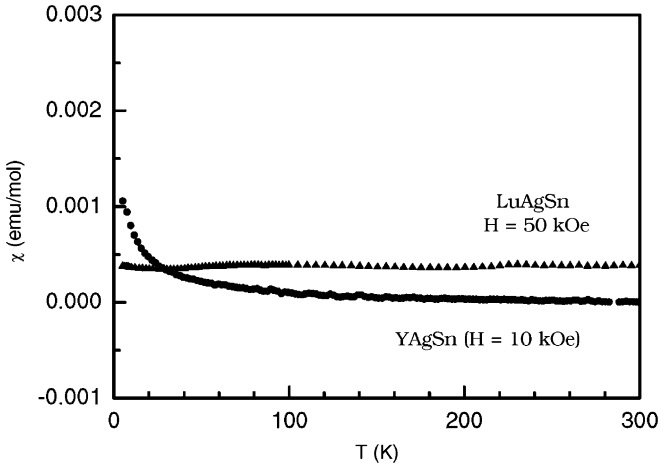

Fig. 6. dc susceptibility of YAgSn and LuAgSn measured at H = 10 and 50 kOe respectively.

Integrations of the COHP up to the Fermi level give ICOHP bonding energies of 1.22 eV/bond and 0.42 eV/bond for Ag–Sn and Ag–Ag, respectively. Thus, the Ag–Sn bonds provide by far the largest portion of bonding energy, but nonetheless also significant Ag–Ag bonding is clearly present in LuAgSn to stabilize the structure.

3.4. Magnetic properties of TmAgSn

In Fig. 5, we show the susceptibility (χ) and inverse susceptibility (χ^{-1}) of TmAgSn measured in a steady field of 10 kOe. There is no magnetic ordering down to a temperature of 2 K. The temperature dependence of χ deviates from Curie-Weiss behavior below 100 K, presumably because of the influence of crystal field effects. The values of the paramagnetic Curie temperature (θ_p) and the effective Bohr magneton number (μ_{eff}) are 17 K and 7.2 μ_B/Tm atom. The value of μ_{eff} is close to the expected value of 7.56 μ_B for a free Tm^{3+} ion. In Fig. 6, we show the susceptibilities of YAgSn and LuAgSn. The susceptibility values remain of the order of 10^{-4} emu/mol in the entire range of the measurement establishing them to be Pauli paramagnets. LuAgSn exhibits an almost temperature independent $\chi(T)$ behavior. The susceptibility of YAgSn slightly increases with decreasing temperature, indicating trace amounts of paramagnetic impurities.

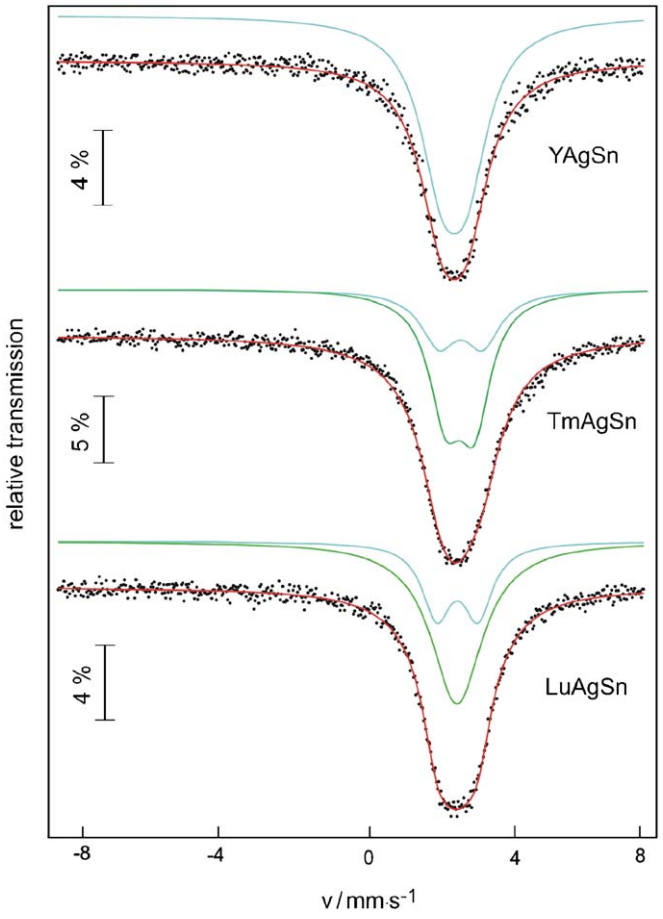

Fig. 7. Experimental and simulated ^{119}Sn Mössbauer spectra of YAgSn, TmAgSn, and LuAgSn at 78 K.

3.5. ^{119}Sn Mössbauer spectroscopy and solid-state NMR

Fig. 7 summarizes the ^{119}Sn Mössbauer spectra of the compounds under study. The hyperfine parameters extracted from these data by least-squares fitting are summarized in Table 5. The spectrum of YAgSn could be fitted with a single quadrupole-split lineshape in excellent agreement with the electric field gradient value predicted from the electric field gradient calculation. The spectra of TmAgSn and LuAgSn can be fitted to superpositions of two quadrupole doublets in the approximate 2:1 ratios predicted from the crystal structure. In the case of the lutetium compound the measured quadrupolar splittings are also found in excellent agreement with the ones predicted from the WIEN2k [44] calculation. In contrast, for the compound TmAgSn good agreement between experiment and calculation is only found for the Sn2 site, while the quadrupolar splitting for the Sn1 site is found significantly smaller than predicted from the crystal structure. We are presently unable to resolve this discrepancy.

Fig. 8 displays the ^{119}Sn solid-state NMR spectra of YAgSn and LuAgSn (no spectrum of the thulium compound can be obtained because of its intrinsic Curie paramagnetism). The spectra reveal the site multiplicities predicted from the structure solutions and show no

Table 5
Fitting parameters of ^{119}Sn Mössbauer measurements for YAgSn, TmAgSn and LuAgSn.

Compound	$\delta 1$	ΔE_{Q1}	$\Gamma 1$	$\delta 2$	ΔE_{Q2}	$\Gamma 2$	Area ratio Sn1/Sn2
YAgSn	1.78(1)	0.43(4) (0.41)	0.91(9)	—	—	—	—
TmAgSn	1.89(1)	0.34(3) (0.65)	0.94(1)	1.91(1)	0.74(2) (0.73)	0.80(9)	26:74
LuAgSn	1.81(3)	0.10(3) (0.17)	0.94(2)	1.83(1)	0.59(2) (0.61)	0.81(5)	33:67

Numbers in parentheses represent the statistical errors in the last digit. δ, isomeric shift; ΔE_Q, electric quadrupole splitting; Γ, experimental line width. All the parameters are in mm/s. The parameters in parentheses are the quadrupole splitting values calculated by Wien2k programme.

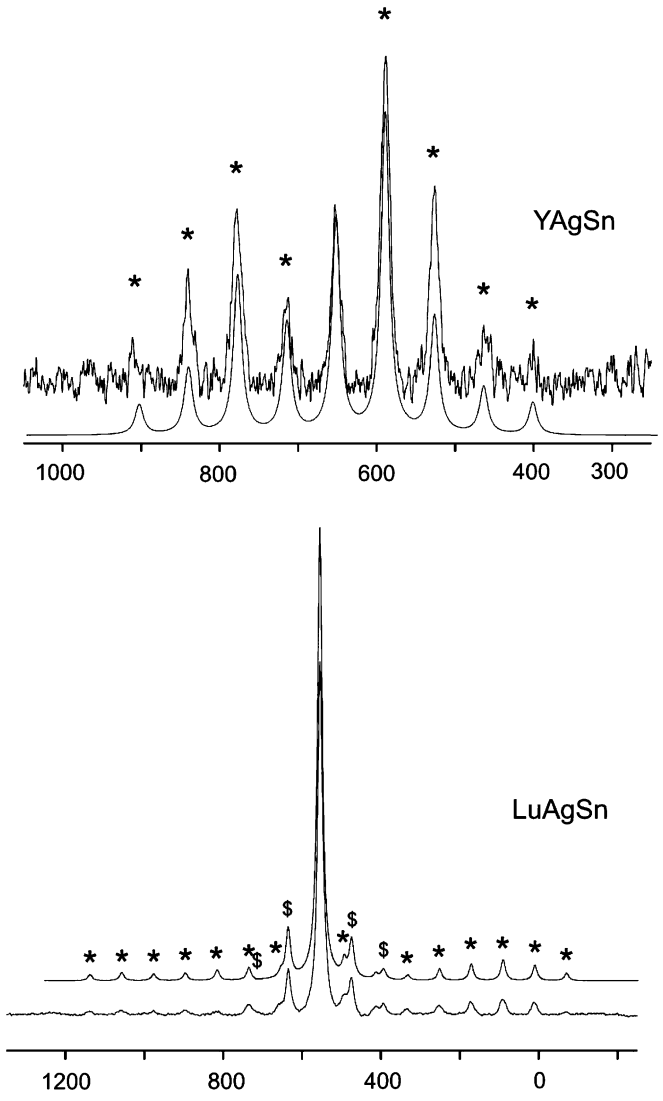

Fig. 8. ^{119}Sn MAS NMR spectra for YAgSn and LuAgSn measured at room temperature (spinning speed 12 kHz). Spinning sidebands are indicated with asterisks and dollar sign for different tin sites.

evidence of any Ag/Sn site disordering. Table 6 summarizes the isotropic and anisotropic magnetic shielding data extracted from these spectra. In the case of YAgSn, a nearly axially symmetric shielding tensor is observed, consistent with the local tin site symmetry ($3m$.) in this compound. For LuAgSn the significant site symmetry difference between the Sn1 site ($\bar{6}$) and the Sn2 site ($\bar{6}2m$) is very clearly manifested in the different magnitudes of the chemical shift anisotropies. For the Sn2 site, the near-zero asymmetry parameter is nicely consistent with the axial local symmetry. Inspection of Tables 5 and 6 suggests that the ^{119}Sn NMR chemical shift anisotropy and the ^{119}Sn Mössbauer quadrupolar splitting are strongly correlated with each other. In concert with additional electric field gradient calculations we are presently examining this relationship for a wider range of intermetallic compounds.

Table 6
^{119}Sn MAS NMR chemical shifts (δ_{iso}) of YAgSn and LuAgSn relative to tetramethyltin.

Compound	site	$\delta_{iso}(^{119}Sn)$ (ppm)	η_{CS}	δ(ppm)	Δ (Hz)
YAgSn	Sn1	649	0.10	270	1770.3
LuAgSn	Sn1	554	0.35	−96	2178.8
	Sn2	412	0.10	913	1971.4

MAS centerband linewidths (FWHH) Δ, chemical shift anisotropy (δ) and asymmetry parameter (η_{CS}) extracted from spectra by using the DMFit routine and using the definitions given in the text are also tabulated.

Acknowledgments

We are grateful to B. Heying and Dipl.-Ing. U. Ch. Rodewald for the intensity data collections on the four-circle diffractometer and to H.-J. Göcke and Dipl.-Chem. F. M. Schappacher for the work on the scanning electron microscope. This work was supported by the Deutsche Forschungsgemeinschaft. S.R. and C.P.S. are indebted to the Alexander-von-Humboldt Foundation and the NRW Graduate School of Chemistry for research stipends. J.P.A. and R.P. acknowledge support from the ESF COST D30 programme.

References

[1] D. Mazzone, D. Rossi, R. Marazza, R. Ferro, J. Less-Common Met. 80 (1981) P47.
[2] A. Adam, J. Sakurai, Y. Yamaguchi, H. Fujiwara, K. Mibu, T. Shinjo, J. Magn. Magn. Mater. 90&91 (1990) 544.
[3] J. Sakurai, S. Nakatani, A. Adam, H. Fujiwara, J. Magn. Magn. Mater. 108 (1992) 143.
[4] W. Bażela, J. Leciejewicz, K. Małetka, A. Szytuła, J. Magn. Magn. Mater. 117 (1992) L1.
[5] W. Bażela, M. Guillot, J. Leciejewicz, K. Małetka, A. Szytuła, J. Magn. Magn. Mater. 140–144 (1995) 1137.
[6] M. Guillot, A. Szytuła, Z. Tomkowicz, R. Zach, J. Alloys Compd. 226 (1995) 131.
[7] Z. Hossain, R. Nagarajan, M. Etilé, C. Godart, J.P. Kappler, L.C. Gupta, R. Vijayaraghavan, J. Magn. Magn. Mater. 150 (1995) 223.
[8] O.V. Zaplatinski, P.S. Salamakha, L.A. Muratova, Inorg. Mater. 32 (1996) 734.
[9] F. Canepa, S. Cirafici, J. Alloys Compd. 232 (1996) 71.
[10] F. Merlo, M. Pani, M.L. Fornasini, J. Alloys Compd. 232 (1996) 289.
[11] M. Lenkewitz, S. Corsépius, G.R. Stewart, J. Alloys Compd. 241 (1996) 121.
[12] R. Pöttgen, J. Alloys Compd. 243 (1996) L1.
[13] K. Katoh, T. Takabatake, A. Minami, I. Oguro, H. Sawa, J. Alloys Compd. 261 (1997) 32.
[14] K. Łątka, E.A. Görlich, W. Chajek, R. Kmieć, A.W.J. Pacyna, J. Alloys Compd. 262–263 (1997) 108.
[15] V. Ivanov, A. Szytuła, J. Alloys Compd. 262–263 (1997) 253.
[16] D.T. Adroja, B.D. Rainford, A.J. Neville, J. Phys.: Condens. Matter 9 (1997) L391.
[17] S. Baran, J. Leciejewicz, N. Stüsser, A. Zygmunt, Y. Ding, J. Magn. Magn. Mater. 170 (1997) 143.
[18] S. Baran, A. Szytuła, J. Leciejewicz, N. Stüsser, Y. Ding, in: M. de Boissieu, J.-L. Verger-Gaugry, R. Currat (Eds.), Aperiodic'97, Proceedings of the International Conference on Aperiodic Crystals,

Alpe d'Huez, August 27–31, World Scientific, Singapore, 1997, pp. 599–603.
[19] E.A. Görlich, K. Łątka, R. Kmieć, W. Warkocki, Mol. Phys. Rep. 22 (1998) 35.
[20] R. Pöttgen, P.E. Arpe, C. Felser, D. Kußmann, R. Müllmann, B.D. Mosel, B. Künnen, G. Kotzyba, J. Solid State Chem. 145 (1999) 668.
[21] D. Kaczorowski, A. Leithe-Jasper, P. Rogl, H. Flandorfer, T. Cichorek, R. Pietri, B. Andraka, Phys. Rev. B 60 (1999) 422.
[22] D. Fus, V. Ivanov, A. Jezierski, B. Penc, A. Szytuła, Acta Phys. Polon. A 98 (2000) 571.
[23] K. Łątka, E.A. Görlich, J. Gurgul, R. Kmieć, Hyperfine Interactions 126 (2000) 299.
[24] A. Szytuła, A. Jezierski, B. Penc, D. Fus, J. Magn. Magn. Mater. 222 (2000) 47.
[25] K. Łątka, Mol. Phys. Rep. 30 (2000) 94.
[26] R. Müllmann, U. Ernet, B.D. Mosel, H. Eckert, R.K. Kremer, R.-D. Hoffmann, R. Pöttgen, J. Mater. Chem. 11 (2001) 1133.
[27] A. Szytuła, D. Fus, B. Penc, A. Jezierski, J. Alloys Compd. 317–318 (2001) 340.
[28] G. Zanicchi, D. Mazzone, P. Riani, R. Marazza, R. Ferro, J. Alloys Compd. 317–318 (2001) 513.
[29] K. Łątka, R. Kmieć, J. Gurgul, J. Alloys Compd. 319 (2001) 43.
[30] D. Mazzone, P. Riani, G. Zanicchi, R. Marazza, R. Ferro, Intermetallics 10 (2002) 801.
[31] K. Łątka, W. Chajec, R. Kmieć, J. Alloys Compd. 383 (2004) 269.
[32] A. Jezierski, A. Szytuła, Mol. Phys. Rep. 40 (2004) 84.
[33] K. Łątka, J. Gurgul, W. Chajec, R. Kmieć, A.W. Pacyna, J. Alloys Compd. 385 (2004) 64.
[34] K. Łątka, J. Gurgul, R. Kmieć, A.W. Pacyna, W. Chajec, J. Alloys Compd. 390 (2005) 9.
[35] R.-D. Hoffmann, R. Pöttgen, Z. Kristallogr. 216 (2001) 127.
[36] C.P. Sebastian, H. Eckert, S. Rayaprol, R.-D. Hoffmann, R. Pöttgen, Solid State Sci. 8 (2006) 560.
[37] C.P. Sebastian, H. Eckert, R.-D. Hoffmann, J.P. Wright, J.P. Attfield, R. Pöttgen, unpublished results.
[38] W. Jeitschko, Acta Crystallogr. B 26 (1970) 815.
[39] R. Pöttgen, Th. Gulden,, A. Simon, GIT-Laborfachzeitschrift 43 (1999) 133.
[40] K. Yvon, W. Jeitschko, E. Parthé, J. Appl. Crystallogr. 10 (1977) 73.
[41] D.A. Perkins, J.P. Attfield, Chem. Commun. 229 (1991).
[42] Brucker, SAINT and SMART Bruker, AXS Inc. Madison, Wisconsin, USA, 2001.
[43] G. M. Sheldrick, SADABS. Version 2.10. Bruker AXS Inc., Madison, Wisconsin, USA, 2003.
[44] P. Blaha, K. Schwarz, G. K. H. Madsen, D. Kvasnicka, J. Luitz, WIEN2k, An Augmented Plane Wave + Local Orbitals Program for Calculating Crystal Properties, Karlheinz Schwarz, Technical Universität Wien, Austria, 2001, ISBN 3–9501031–2.
[45] D. Massiot, DMFIT program; available at http://crmht-europe.cnrs-orleans.fr
[46] O. K. Andersen, O. Jepsen, Tight-Binding LMTO Vers. 4.7, Max-Planck-Institut für Festkörperforschung, Stuttgart, 1994.
[47] O.K. Andersen, O. Jepsen, M. Sob, in: M. Yussouff (Ed.), Electronic Band Structure and its Applications, Lecture Notes in Physics, Vol. 283, Springer, Berlin, 1987, p. 1.
[48] H.L. Skriver, The LMTO Method—Muffin Tin Orbitals and Electronic Structure, Springer, Berlin, 1984.
[49] P.E. Blöchl, O. Jepsen, O.K. Andersen, Phys. Rev. B 49 (1994) 16223.
[50] W.R.L. Lambrecht, O.K. Andersen, Phys. Rev. B 34 (1986) 2439.
[51] R. Dronskowski, P.E. Blöchl, J. Phys. Chem. 97 (1993) 8617.
[52] G. M. Sheldrick, SHELXL-97, Program for Crystal Structure Refinement, University of Göttingen, Germany, 1997.
[53] H.D. Flack, G. Bernadinelli, Acta Crystallogr. A 55 (1999) 908.
[54] H.D. Flack, G. Bernadinelli, J. Appl. Crystallogr. 33 (2000) 1143.
[55] S. Rayaprol, C. P. Sebastian, R. Pöttgen, J. Solid State Chem., in press.
[56] B. Gibson, R. Pöttgen, R.K. Kremer, A. Simon, K.R.A. Ziebeck, J. Alloys Compd. 239 (1996) 34.
[57] J. Emsley, The Elements, Oxford University Press, Oxford, 1999.
[58] J. Donohue, The Structures of the Elements, Wiley, New York, 1974.
[59] E. Parthé, L. Gelato, B. Chabot, M. Penzo, K. Cenzual, R. Gladyshevskii, TYPIX — Standardized Data and Crystal Chemical Characterization of Inorganic Structure Types, Gmelin Handbook of Inorganic and Organometallic Chemistry, eighth ed., Springer, Berlin, 1993.
[60] M.F. Zumdick, R. Pöttgen, Z. Kristallogr. 214 (1999) 90.